Facile synthesis of $C_3N_4/NiIn_2S_4$ heterostructure with novel solar steam evaporation efficiency and photocatalytic H_2O_2 production performance

Anhu Wang [a,b], Huagen Liang [a,b,*], Fu Chen [a,*], Xinlong Tian [c,*], Shibin Yin [d], Shengyu Jing [e], Panagiotis Tsiakaras [f,*]

[a] Jiangsu Key Laboratory of Coal-based Greenhouse Gas Control and Utilization, Low Carbon Energy Institute, China University of Mining and Technology, Xuzhou 221008, China
[b] School of Materials Science and Engineering, China University of Mining and Technology, Xuzhou 221008, China
[c] State Key Laboratory of Marine Resource Utilization in South China Sea, Hainan Provincial Key Lab of Fine Chemistry, School of Chemical Engineering and Technology, Hainan University, Haikou 570228, China
[d] MOE Key Laboratory of new Processing Technology for non-ferrous Metals and Materials, Guangxi Key Laboratory of Processing for non-ferrous Metals and Featured Materials, Guangxi University, Nanning, Guangxi, China
[e] School of Information and Control Engineering, China University of Mining and Technology, Xuzhou, Jiangsu 221008, China
[f] Laboratory of Alternative Energy Conversion Systems, Department of Mechanical Engineering, School of Engineering, University of Thessaly, Pedion Areos, 38834, Greece

ARTICLE INFO

ABSTRACT

Using solar energy to obtain valuable fresh water through interface evaporation is a promising environmentally friendly technology. However, the organic pollutants in wastewater may cause potential water safety hazards. The removal of organic pollutants by H_2O_2 in-situ generated photocatalytically is an effective means to achieve water purification. In this work, a simple method is proposed for the controllable synthesis of $C_3N_4/NiIn_2S_4$ heterojunction, by which can be achieved both the efficient evaporation of the solar interface and the photocatalytic production of H_2O_2. The evaporation rate and solar evaporation efficiency of $C_3N_4/NiIn_2S_4$ reach up to 3.25 kg·m^{-2}·h^{-1} and 215.06%, respectively, under the irradiation of one sun (1 kW·m^{-2}). Furthermore, $C_3N_4/NiIn_2S_4$ heterojunction exhibits an excellent photocatalytic H_2O_2 production activity of 1080 μmol^{-1}·L^{-1}·h^{-1}. This study provides a facile and attractive strategy for the design of photothermal materials and photocatalysts with efficient interfacial evaporation and sewage purification, especially for complex sewage samples.

1. Introduction

The shortage of freshwater resources is now a common global problem. Although around 70% of the world is covered by water, only 0.01% of this is available to mankind, excluding hard to use fresh water such as polar glaciers [1]. In the face of the shortage of freshwater resources, various methods of purifying fresh water have been reported. For example, ion exchange is used to purify seawater by removing salts through ion exchange membranes, which can remove salts to a greater extent, but the complex structure of the device is not conducive to operation. Another example is distillation, where external energy is used to promote the evaporation of water to obtain excellent water quality, but the overall energy consumption is high. Methods such as these for obtaining fresh water have a high energy requirement and run counter to the concept of green sustainability, with energy being provided

mainly by non-renewable fossil fuels. For this reason, evaporation condensation and harvesting of freshwater resources through the evaporation of photothermal water from the most abundant renewable resource, solar energy, is now one of the most important methods.

When the solar photothermal water evaporates, the hydrogen bonds between the liquid water molecules break and thus become gaseous, while the hydrogen bonding network will reform after the condensation, namely when the water vapor condenses into liquid water. In addition to temperature and pressure which can change the state of water, the phase behavior of water can also be changed by introducing substances which interact with the water molecules, i.e., by changing the hydrogen bonding network between the water molecules so that the forces between the water molecules are weakened and the latent heat of evaporation (enthalpy of evaporation/energy required for evaporation) is reduced [2]. Traditional photothermal water evaporation, by

photothermal materials, can be divided into three kinds according to the different positions of photothermal materials in the water body; at the bottom of the heating, and water-air interface heating [3]. The third type of interfacial evaporation method, in which the photothermal material is at the interface between solution and air, effectively solves the problems encountered in the first two methods. In the interface solar photothermal water evaporation technology, the photothermal material is used to absorb solar energy, therefore, the location of the absorbed solar energy converted into heat by the photothermal material, and the area of steam generation are concentrated at the interface between water and air. In this way, only the water at the interface is locally heated, so that the temperature of the water body tends to the ambient temperature, which effectively reduces the heat loss while improving the photothermal conversion efficiency [4,5].

Transition metal chalcogenides (MS_x) generate electron hole defects during their synthesis, which cause surface carriers to leap, producing a plasmonic resonance effect similar to that of precious metal photothermal materials, converting the absorbed light into heat and releasing it [6]. The MS_x have a stronger light absorption in the near-infrared region than conventional wide-bandgap semiconductor materials, allowing for more efficient use of sunlight. In addition, MS_x can maintain good photothermal stability under long-term light exposure. MS_x are currently available in a wide range of materials, simple to prepare and easy to compound. Therefore, for all the above reasons, they have been widely studied in the field of photothermal conversion. Ding et al. [7] successfully synthesized MoS_2 (MoS_2-Cys) nanospheres with an average diameter of about 422 nm modified by L-cysteine by a facile method, which exhibited good light absorption in the near-infrared region. Under irradiation with an 808 nm laser at a power density of 0.8 W·cm^{-2}, the photothermal conversion efficiency of MoS_2-Cys was calculated to be 35.0% at concentrations as low as 50 μg·mL^{-1}, which is much higher than that of similar materials reported at the same irradiation dose and power. Liu et al. [8] prepared a g-C_3N_4 nanosheet modified by copper sulphide (CuS) nanoparticles with a hydrothermal method, called PEG-CuS@g-C_3N_4 photothermal composite. Characterization tests revealed that the nanoparticles of CuS did not show significant agglomeration and showed a uniform distribution. In addition, the temperature of the dispersions with a concentration of 200 μg·mL^{-1} was irradiated with an 808 nm laser at a power of 2.5 W·cm^{-2} and increased by about 25.0 °C due to the strong near-infrared absorption properties of the PEG-CuS@g-C_3N_4 photothermal composite. Its photothermal conversion efficiency reached 59.64%, demonstrating good photothermal performance. However, now, the solar interface evaporation faces some problems, e.g., several times increase in the solar intensity or multi-layer components were needed to achieve a satisfactory evaporation efficiency. In addition, most of the photothermal evaporation experiments reported in the literature are built by coating powder samples on hydrophilic substrates or construction of three-dimensional self-standing structures, and as a result, they float on the water. However, in both cases, there could be a risk of structural collapse and the photothermal materials fall into the water. This may not only reduce the efficiency of photothermal evaporation, but also cause secondary pollution of water. At this time, if the photothermal material also has a certain photocatalytic ability for H_2O_2 generation, the fallen photothermal material could further enhance the role of water purification [9].

H_2O_2 has important applications in environmental remediation as a clean oxidant, and the annual demand is huge [10,11]. This has led to the exploration of various H_2O_2 production technologies. Common technologies include conventional anthraquinone oxidation method [12], electrochemical reactions [13], photocatalytic reactions [14], and direct catalytic reactions of H_2 and O_2 [15]. Among them, photocatalysis is considered as a simple, green, sustainable, and low-energy strategy for H_2O_2 production, which can be achieved by using only renewable solar energy as power input, water and O_2 as feedstock, and requires the use of suitable semiconductors as photocatalysts [16]. The main challenges in developing photocatalysts are to improve the response to visible light, to

enhance the efficiency of separation and transport of photogenerated electron-hole pairs, and to promote the reduction kinetics of O_2 to form H_2O_2 on the photocatalyst surface [17,18]. So far, a wide variety of semiconductor photocatalysts have been investigated [19,20]. The C_3N_4-based materials have excellent bifunctional activity for solar-driven interfacial water evaporation and photocatalytic H_2O_2 production [21]. The g-C_3N_4/MoS_2 floating solar stills studied by Gan et al. can achieve a water evaporation rate of 1.23 kg·m^{-2}·h^{-1} under the irradiation of one sun intensity [22]. In addition, NiCoP-decorated g-C_3N_4 was utilized as an efficient photocatalyst with excellent H_2O_2 production capability. NiCoP presents better electronic conductivity and electronic structure, which when inter-loaded with g-C_3N_4 not only enhance the absorption of visible light, but also reduces the recombination rate of electrons and holes, providing more active sites [23].

In this work, we synthesized a highly efficient C_3N_4/$NiIn_2S_4$ composite with dual function (kill two birds with one stone) by using a one-step solvothermal method. Due to the addition of $NiIn_2S_4$, the visible light absorption capacity of the composite was significantly enhanced, while it also effectively inhibited the recombination of carrier pairs and provided more active sites. In this way, it not only achieves a water evaporation rate of 3.25 kg·m^{-2}·h^{-1} under the irradiation of one sun intensity (100 mW·cm^{-2}), but it is also able to produce 1080 μmol^{-1}·L^{-1} of H_2O_2 in 1 h under visible light (λ > 420 nm) irradiation.

2. Experimental and methods

2.1. Chemicals and materials

The reagents used in this experiment were as follows: melamine (AR) purchased from Tianjin Comio Chemical Reagent Co., thiourea (CH_4N_2S, AR) purchased from Shanghai Qingshun Chemical Reagent Co., potassium hydrogen phthalate ($C_8H_5KO_4$, AR, 99.8%), nickel chloride ($NiCl_2·6 H_2O$, AR, 99%), indium chloride ($InCl_3$, AR, 99.9%), potassium iodide (KI, AR, 99%), and ethylene glycol ($C_2H_6O_2$, AR, 98%) purchased from Shanghai Maclean Biochemical Technology Co., and N,N-dimethylformamide (C_3H_7NO, AR) and anhydrous ethanol (C_2H_5O, AR) purchased from Taicang Huxiang Reagent Co. The water used in the experiments was in all cases deionized water.

2.2. Synthesis of C_3N_4

C_3N_4 was synthesized by thermal polycondensation. An appropriate amount of melamine was put into an alumina ceramic crucible with a cover and heated to 550 °C at a rate of 5 °C min^{-1} in a muffle furnace for 4 h. After cooling to room temperature, yellow product (C_3N_4) was obtained.

2.3. Synthesis of C_3N_4/$NiIn_2S_4$

The procedure of the synthesis of C_3N_4/$NiIn_2S_4$ hybrids is shown in Scheme 1.

Typically, 1 mmol of $NiCl_2·6 H_2O$, 2 mmol of $InCl_3$, and excess thiourea were weighed and dissolved in 20 mL of a mixture of N, N-dimethylformamide (DMF) and ethylene glycol (EG) (V_{DMF}: V_{EG}=1:1), and then 45 mg powder of the above-prepared C_3N_4 prepared above was dropped into the mixture and ultrasonically dispersed for 30 min. Finally, the resulting suspension was poured into a polytetrafluoroethylene-lined high pressure reactor and held at 200 °C for 24 h. After cooling to room temperature in the oven, the reaction material was centrifuged at 8000 rpm for 5 min to obtain the precipitate, and the precipitate was washed several times with deionized water and anhydrous ethanol, respectively. After that, the resulting product was dried under vacuum at 60 °C for 8 h. For comparison, C_3N_4/Ni_3S_4 and C_3N_4/In_2S_3 were also prepared, following the same conditions without adding $InCl_3$ or $NiCl_2·6 H_2O$, respectively.
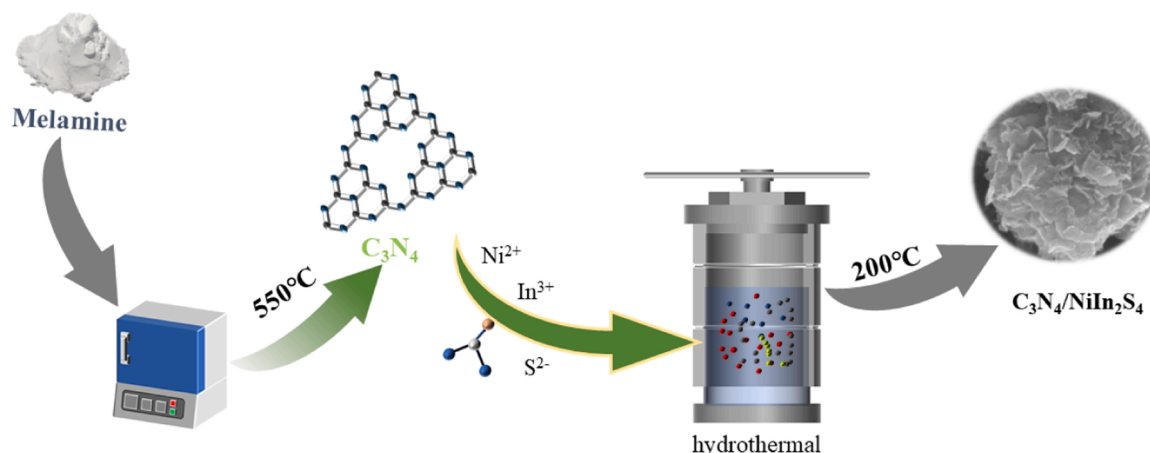
Scheme 1. The preparation process used to fabricate the $C_3N_4/NiIn_2S_4$ composite.

2.4. Characterization of the materials

The crystalline structure of the as-synthesized materials was examined by X-ray diffraction spectroscopy (XRD, Bruker D8-Advance X-ray diffractometer) using Cu-Kα radiation. A high-resolution scanning electron microscope (FSEM, MAIA3 LMH TESCAN) was used to study the structure and morphology of the materials. A valuable quantitative and chemical state information for the materials surface was obtained using X-ray photoelectron spectroscopy (XPS, ESCALAB 250Xi spherical analyzer) with Al $K_α$ radiation. The UV-Vis diffuse reflectance spectra (DRS) were measured employing a UV-Vis spectrophotometer (Lambda 950) with a wavelength range of 200–900 nm and using $BaSO_4$ as a reference. Fourier transforms infrared spectra (FT-IR) were taken with a Bruker VEC-TORTM 22 FTIR spectrometer within the region of 500–4000 cm^{-1}. The contact angle is derived from Dataphysics-OCA20.

2.5. Solar water evaporation experiment

As shown in Scheme 2 and Fig. S1, the solar water evaporation device consists of water container, evaporator, simulated sunlight, and electronic balance. The water container is a polypropylene beaker, which has a low thermal conductivity. The hollow circular insulation foam was positioned on the top of the beaker, to provide insulation and avoid direct sunlight to the water surface to affect the experimental results, while its center was passed-through the skimmed cotton as a water supply channel.
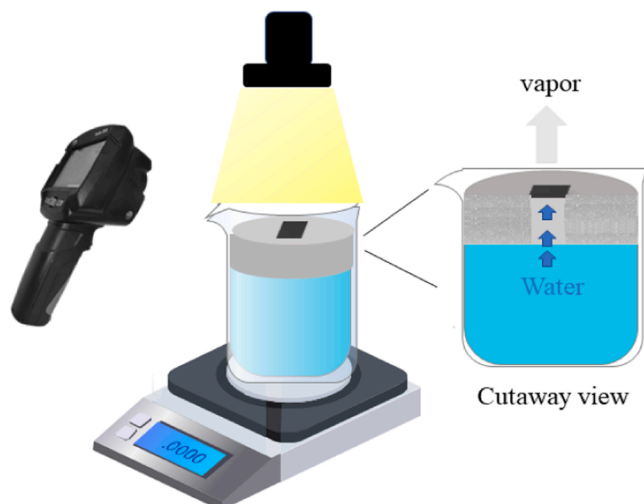
The as-prepared powder sample was coated at the top of the skimmed cotton with an effective area of 4 cm^2 (2 cm × 2 cm), and the loading of powder sample was 12.5 mg·cm^{-2}, as shown in Fig. S2. An electronic balance (Sartorius BASA 124 S-CW) was used to record the quality change of water. A 300 W xenon lamp with a light intensity of one sunlight (100 mW·cm^{-2}) was used as the simulated solar light source. Throughout the evaporation of the solar photothermal water, the photothermal material indicating the temperature change process was recorded using an infrared thermographic camera (Testo 869).

2.6. Photocatalytic H_2O_2 production test

Typically, 20 mg of the as-prepared catalyst was added to a mixture of 45 mL of water and 5 mL of ethanol. The suspension was then sonicated for 10 min at room temperature. Photocatalytic H_2O_2 production was carried out for 60 min under O_2 equilibrium conditions with a 300 W xenon lamp (λ > 420 nm) at about 1time the solar light intensity (100 mW·cm^{-1}). Prior to the photoreaction, O_2 was passed through for 30 min to reach O_2 adsorption/desorption equilibrium. During illumination, 3 mL of the solution were taken every 15 min and the catalyst was removed using a 0.45 μm filter. The amount of H_2O_2 was analyzed by iodometry. In general, 1 mL of the previously obtained solution was placed in a 5 mL centrifugal tube, 1 mL of 0.1 mol·L^{-1} aqueous potassium hydrogen phthalate ($C_8H_5KO_4$) was added, followed by 1 mL of 0.4 mol·L^{-1} aqueous potassium iodide (KI) [24]. Finally, it was allowed to stand for 30 min, and the absorbance of the mixed solution at 350 nm was measured using UV–vis spectrometer (METASH UV-5500PC).

2.7. Photoelectrochemical characterization

The working electrode was prepared by mixing 2 mg of the prepared material with 200 μl of ethanol and 5 μl of Nafion reagent to form a paste and then applying the slurry dropwise to the conductive surface of the FTO (Fluorine Tin Oxide) glass plate, covering an area of about 1 cm^2 (1 cm × 1 cm). A conventional three-electrode electrolytic cell was used, in which a saturated calomel electrode and a platinum electrode were used as reference and auxiliary electrodes, respectively. The photoelectrochemical measurements were performed at room temperature, with 0.1 M Na_2SO_4 solution used as an electrolyte and deoxygenated by passing N_2 for 30 min, with a CHI 660d electrochemical workstation (Shanghai Chenhua Instruments Co., Ltd., China). Electrochemical impedance spectroscopy (EIS) was applied in a Na_2SO_4 solution at a potential of 0.2 V, an AC amplitude of 2 mV and a frequency range of 10 kHz to 100 mHz.

Scheme 2. Schematic diagram of the solar water evaporation unit.

3. Results and discussion

3.1. Materials characterization

As can be seen from Fig. 1a, the characteristic peaks, belonging to the (100) and (002) crystal planes of C_3N_4, appear at around 13.1° and 27.6° in the XRD patterns of all the prepared composites and pure C_3N_4 samples [25]. The XRD patterns also show the diffraction crystallographic surfaces of (220), (311), (400), (422), (511), and (440), which belong to the $NiIn_2S_4$ phase (JCPDS card No. 70–2900).

In this work, C_3N_4/Ni_3S_4 and C_3N_4/In_2S_3 were prepared for comparison by using a similar solvothermal process, where nickel sulfide showed characteristic peaks belonging to the (111), (220), (311), (400), (422), (511), and (440) crystal planes with a crystal structure consistent with the Ni_3S_4 spinel (JCPDS No. 76–1813), while indium sulfide shows characteristic peaks belonging to the (111), (220), (311), (222), (400),

(511), (440), (531), and (533) crystal planes, and its crystalline structure is consistent with In_2S_3 (JCPDS No. 65–0459). The above findings confirm the successful synthesis of the samples.

The as-prepared C_3N_4 is shown in Fig. 1b as a bulk of about 18 μm in size with a relatively smooth surface. Both In_2S_3 (Fig. 1c) and Ni_3S_4 (Fig. 1d) are uniformly coated on the C_3N_4 matrix in a lamellar and cluster structure, respectively. In contrast, $NiIn_2S_4$ grows on the C_3N_4 substrate with a more delicate lamellar structure, exposing more pore structure (Fig. 1e).

The most porous structure indicates a high surface area with more exposed active sites, which provides favorable evidence that $C_3N_4/NiIn_2S_4$ has better solar interfacial water evaporation performance and efficient visible light catalysis for H_2O_2 production. From the EDS energy spectrum of the $C_3N_4/NiIn_2S_4$ (Fig. 1f), it is revealed that Ni, In, and S elements are uniformly distributed on the C_3N_4 matrix, which proves that $NiIn_2S_4$ is uniformly grown onto the C_3N_4 matrix. It can also be seen
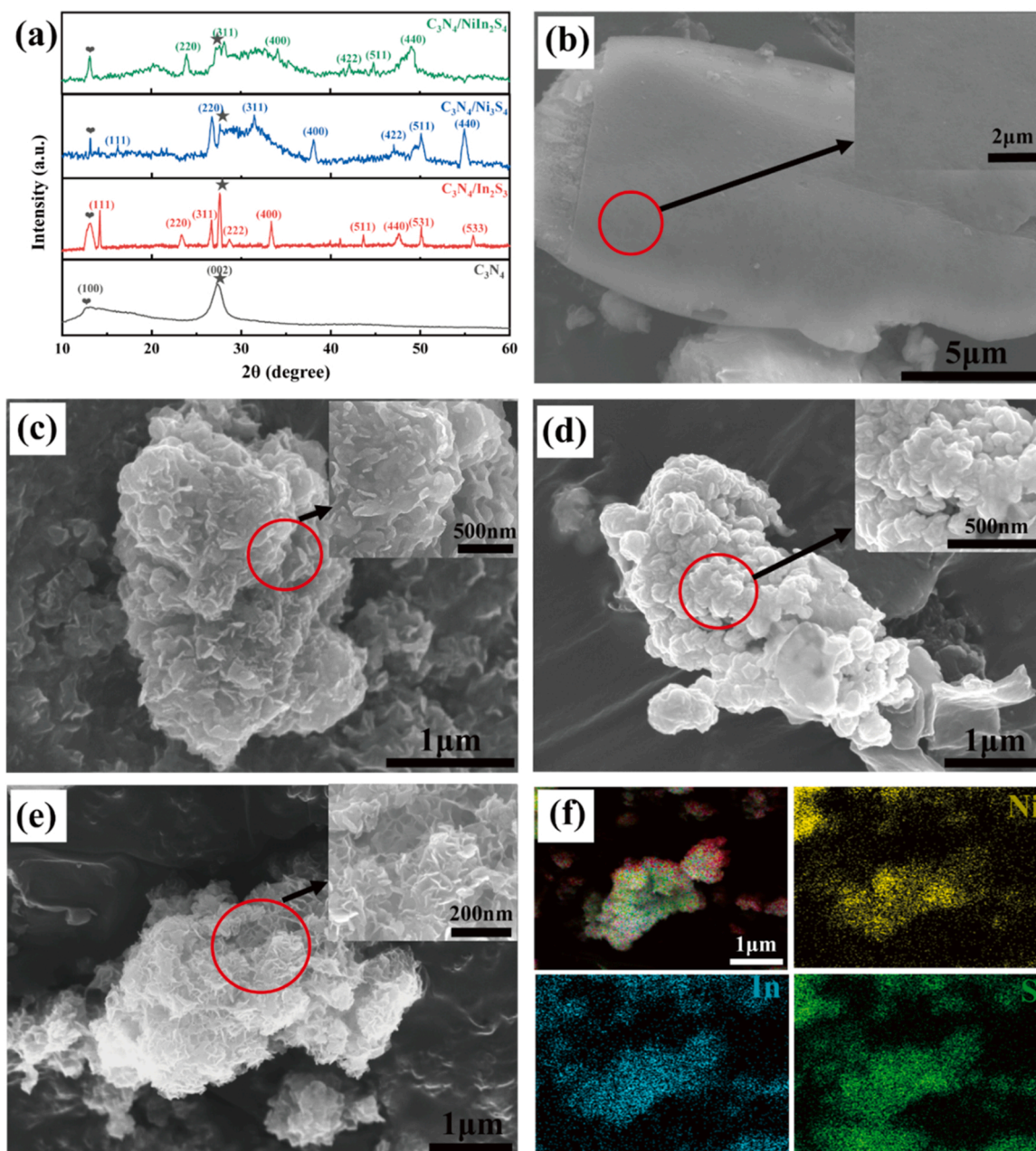

Fig. 1. The XRD pattern of different samples (a); SEM images of the C_3N_4 (b), C_3N_4/In_2S_3 (c), C_3N_4/Ni_3S_4 (d) and $C_3N_4/NiIn_2S_4$ (e); EDS spectrum of $C_3N_4/NiIn_2S_4$ (f).

from Fig. S3 that all the corresponding elements are uniformly distributed in the C_3N_4/In_2S_3 and C_3N_4/Ni_3S_4 composites, which proves the successful preparation of the composites. The surface properties of $C_3N_4/NiIn_2S_4$ were measured by XPS. The Ni, In, and S elements presented in the Ni 2p, In 3d, and S 2p spectra and in the XPS full spectrum, were fitted with a Gaussian fit method, as displayed in Fig. S2. In the Ni 2p spectrum of $C_3N_4/NiIn_2S_4$ (Fig. 2a), two pairs of signals are identified as Ni^{3+} (855.6 and 873.1 eV) and Ni^{2+} (861.2 and 879.2 eV), implying the coexistence of mixed valence states [26].

For the In 3d spectrum (Fig. 2b), two peaks at 443.9 and 451.4 eV correspond to the $3d_{5/2}$ and $3d_{3/2}$ core levels of In^{3+} [27]. In the high-resolution spectrum of S 2p. The $2p3/2$ and $2p1/2$ core levels at 160.5 and 161.6 eV are due to the vibration of the M-S bonds (M = Ni and In) (Fig. 2c). [28,29]. The peak at 167.8 eV can be indexed to the S-O species, because of the partial oxidation [30,31]. Furthermore, the C-S-C bond shows a characteristic peak at 162.8 eV, suggesting that the C element in C_3N_4 was successfully doped to the S atom [29].

Fig. 2d shows the high resolution XPS spectra of C 1 s. The peak 284.8 eV belongs to C-C bond, and 287.5 eV belongs to N-C=N bond [32]. All the above XPS results confirm that Ni^{2+}, Ni^{3+}, and In^{3+} cations, S^{2-} anions, and M-S and N-C≡N bonds are present in $C_3N_4/NiIn_2S_4$, therefore the formation of $NiIn_2S_4$ phase is further confirmed by this. As mentioned above, the transition group metal Ni is present here in the oxidized form with some variable valence capability and therefore has in electron transport in the photocatalytic reaction.

3.2. Solar-driven interfacial evaporation performance

The characteristic vibrational peaks of C_3N_4 are found in the FTIR spectra of the prepared samples (Fig. 3a), which are the broad peaks located at 3000–3500 cm^{-1} belong to the absorption band of N-H stretching and bending vibrations; the characteristic peaks at 1245–1646 cm^{-1} belonging to the absorption band of C-N heterocyclic ring of stretching vibrations and the absorption band of 3-S-homogeneous triazine ring of bending vibrations located at 800–910 cm^{-1} [33,34]. Fig. 3b shows the UV–vis absorption spectra of the prepared materials, and as can be seen the pure C_3N_4 exhibits the weakest ability to absorb light, and $C_3N_4/NiIn_2S_4$ has the strongest ability to absorb light with the widest absorption edge. In the wavelength range from 270 to 510 nm, although the absorption ability of C_3N_4/Ni_3S_4 is weaker than that of C_3N_4/In_2S_3, at wavelengths higher than 500 nm, the sustained light absorption ability of C_3N_4/Ni_3S_4 is stronger than that of C_3N_4/In_2S_3, and its absorption edge is also larger than that of C_3N_4/In_2S_3.

Attributed to its excellent UV–vis light absorption and its intrinsic absorption ability because the sample is black (Fig. S2), $C_3N_4/NiIn_2S_4$ has good solar energy conversion performance. In about 70 s, $C_3N_4/NiIn_2S_4$ reaches a stable temperature (~45 °C) at one sun intensity (Fig. 3c).

The temperature of the evaporated water at one sun intensity for the blank and each of the prepared samples is shown in Fig. 3d, where all reactors reached their maximum temperature at 5 min. The contact-angle test shows that at 0.2 s of droplet drop, the contact angle of $C_3N_4/NiIn_2S_4$ is 13.8°, which is much smaller than C_3N_4 (35.6°), C_3N_4/In_2S_3 (27.8°), and C_3N_4/Ni_3S_4 (26.9°) (Fig. S5). This indicates that $C_3N_4/NiIn_2S_4$ has the best water wettability.

Under the irradiation of a 300 W xenon lamp simulating one sun intensity (100 mW·cm^{-2}), the amount of water vapor produced by the blank control after three hours was 0.49 kg·m^{-2}, and the amount of water vapor produced by pure C_3N_4 and pure $NiIn_2S_4$ was 1.05 kg·m^{-2} and 1.78 kg·m^{-2}, respectively (Fig. S6d). $C_3N_4/NiIn_2S_4$ showed the best solar water evaporation performance with 3.89 kg·m^{-2} of evaporated water in three hours when the dosing amount of C_3N_4 was 45 mg (Fig. S6a).

Under the same conditions, the comparison samples C_3N_4/In_2S_3 and C_3N_4/Ni_3S_4 produced 1.47 and 2.41 kg·m^{-2} of evaporated water in
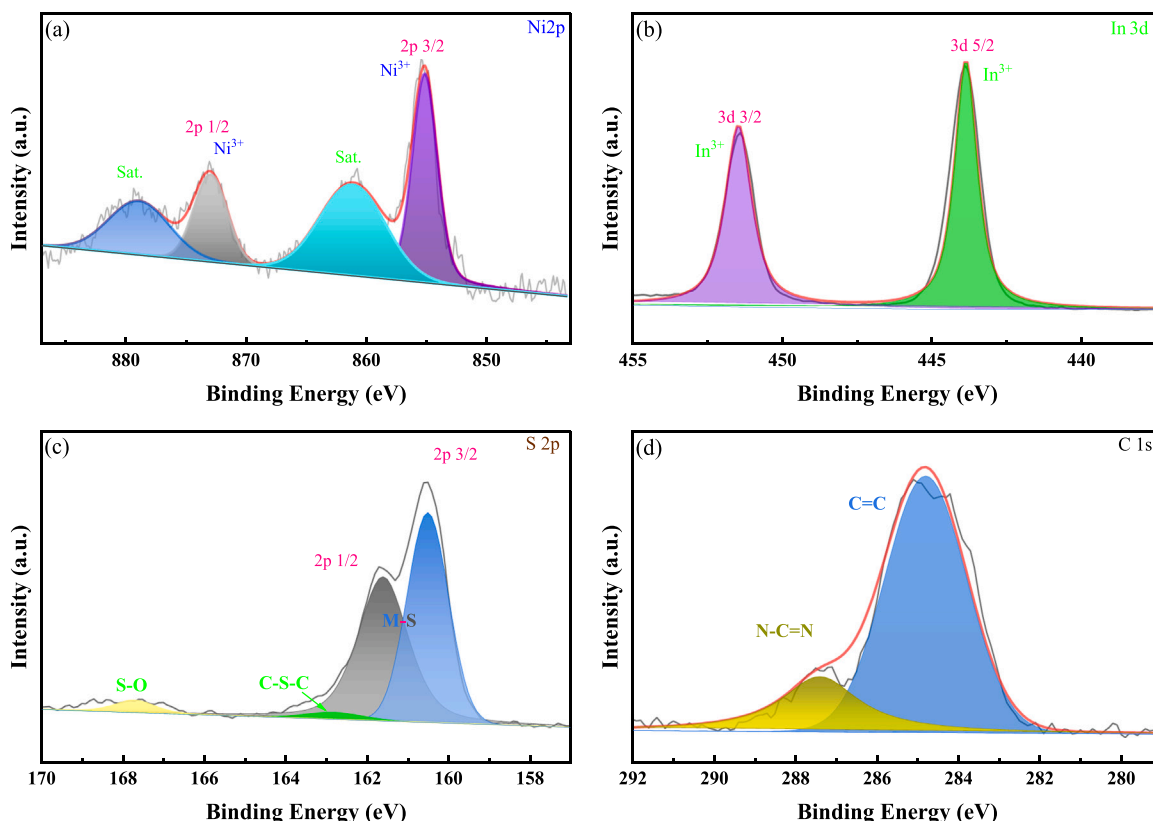
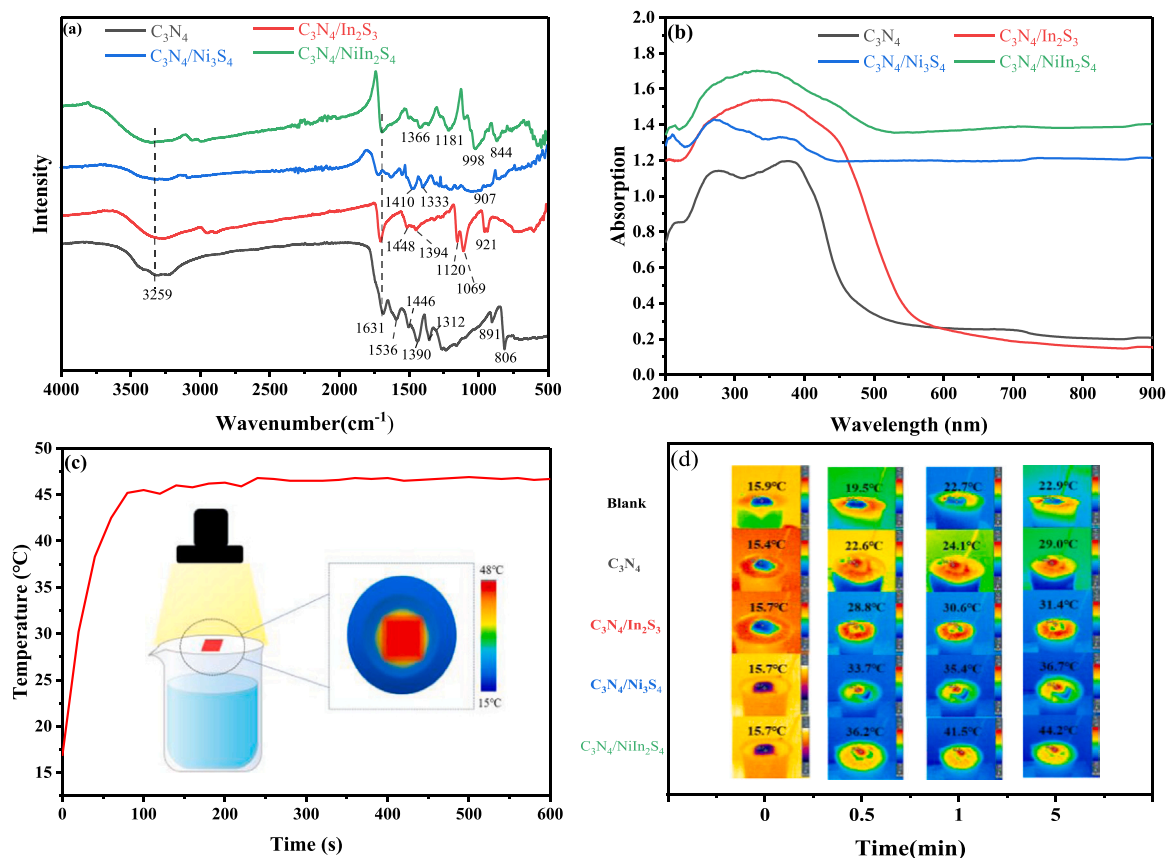**Fig. 2.** High-resolution XPS spectra of Ni 2p (a), In 3d (b), S 2p (c), and C 1 s (d).

Fig. 3. The FTIR spectra of C_3N_4, C_3N_4/In_2S_3, C_3N_4/Ni_3S_4 and $C_3N_4/NiIn_2S_4$ (a); Absorption spectra of C_3N_4, C_3N_4/In_2S_3, C_3N_4/Ni_3S_4 and $C_3N_4/NiIn_2S_4$ at wavelengths of 200–900 nm (b); Temperature change of $C_3N_4/NiIn_2S_4$ under the irradiation of a 300 W xenon lamp with a light intensity of 100 mW·cm^{-1} (c), illustration shows its schematic; The temperatures of Blank, C_3N_4, C_3N_4/In_2S_3, C_3N_4/Ni_3S_4 and $C_3N_4/NiIn_2S_4$ during the experiment (d).

three hours, respectively (Fig. 4a). As shown in Fig. 4b, the water evaporation rate of $C_3N_4/NiIn_2S_4$ is about 3.25 kg·m^{-2}·h^{-1}, which is the fastest rate of water evaporation in this work. Fig. 4c displays the solar water evaporation performance measured in this work is compared with the water evaporation rates, obtained on powder samples, reported in literature the last three years.

Until today, the maximum evaporation rate value of powder samples reported in the literature was less than 2.5 kg·m^{-2}·h^{-1}, while in the present work was found to be 3.25 kg·m^{-2}·h^{-1}. From Fig. 4c, it is revealed that the solar water evaporation performance of $C_3N_4/NiIn_2S_4$ is relatively excellent. In addition, to investigate the stability of the $C_3N_4/NiIn_2S_4$ performance, six cycle experiments were done under the same conditions. The results showed that $C_3N_4/NiIn_2S_4$ has excellent cycle stability and can maintain a water evaporation rate of about 3.24 kg·m^{-2}·h^{-1} in all six experiments (Fig. S6b).

To evaluate the ability of solar water evaporation, the solar to steam conversion efficiency was calculated by the following equations [42]:

$$\eta = \frac{mH_f}{Q} \times 100\% \tag{1}$$

where m is the rate of water vapor production at steady state (kg·m^{-2}·h^{-1}), H_f is the enthalpy of evaporation of water vapor (kJ·kg^{-1}), and Q is the luminous flux (3600 kJ·m^{-2}·h^{-1}).

$$H_f = H_v + (C_w - C_v) \times (T_2 - T_1) \tag{2}$$

where H_v is the heat of vaporization of water at standard atmospheric pressure (2260 kJ·kg^{-1}), C_w (4.18 kJ·kg^{-1}·K) and C_v (1.85 kJ·kg^{-1}·K) are the specific heat capacities of water and water vapor, respectively, T_2 is the boiling point of water at standard atmospheric pressure (283.15 K), and T_1 is the surface temperature of the sample during the

experiment. From this equation, the solar water evaporation efficiency of $C_3N_4/NiIn_2S_4$ at one sun intensity is calculated as 215.06% (Fig. 4d). Moreover, the solar water evaporation efficiency of pure C_3N_4 and $NiIn_2S_4$ is only 58.49% and 95.71%, respectively, which is much smaller than that of $C_3N_4/NiIn_2S_4$ (Fig. S6c).

3.3. Photocatalytic generation of H_2O_2 and photoelectrochemical properties

Furthermore, the ability of each composite to produce H_2O_2 under visible light ($\lambda > 420$ nm) was tested in this work, and the results showed that $C_3N_4/NiIn_2S_4$ produced 1080 μmol^{-1}·L^{-1} of H_2O_2 within 1 h of visible light irradiation (Fig. 5a).

The rate of H_2O_2 production by $C_3N_4/NiIn_2S_4$ was found to be 18.12 μmol^{-1}·L^{-1}·min^{-1} (Fig. 5b); the whole H_2O_2 production process may have two pathways as follows [43]:

$$H_2O + \frac{1}{2}O_2 \xrightarrow{h\nu} H_2O_2 \tag{3}$$

$$H_2O + 2h^+ \rightarrow \frac{1}{2}O_2 + 2H^+ \tag{4}$$

$$O_2 + 2H^+ + 2e^- \rightarrow H_2O_2 \tag{5}$$

$$O_2 + e^- \rightarrow \cdot O_2^- \tag{6}$$

$$\cdot O_2^- + e^- + 2H^+ \rightarrow H_2O_2 \tag{7}$$

As shown in the above equations, H_2O_2 is produced by a photocatalyst promoting the reduction of O_2. In the valence band of a photocatalyst, the holes oxidize H_2O to H^+ and O_2, while the e$^-$ in the
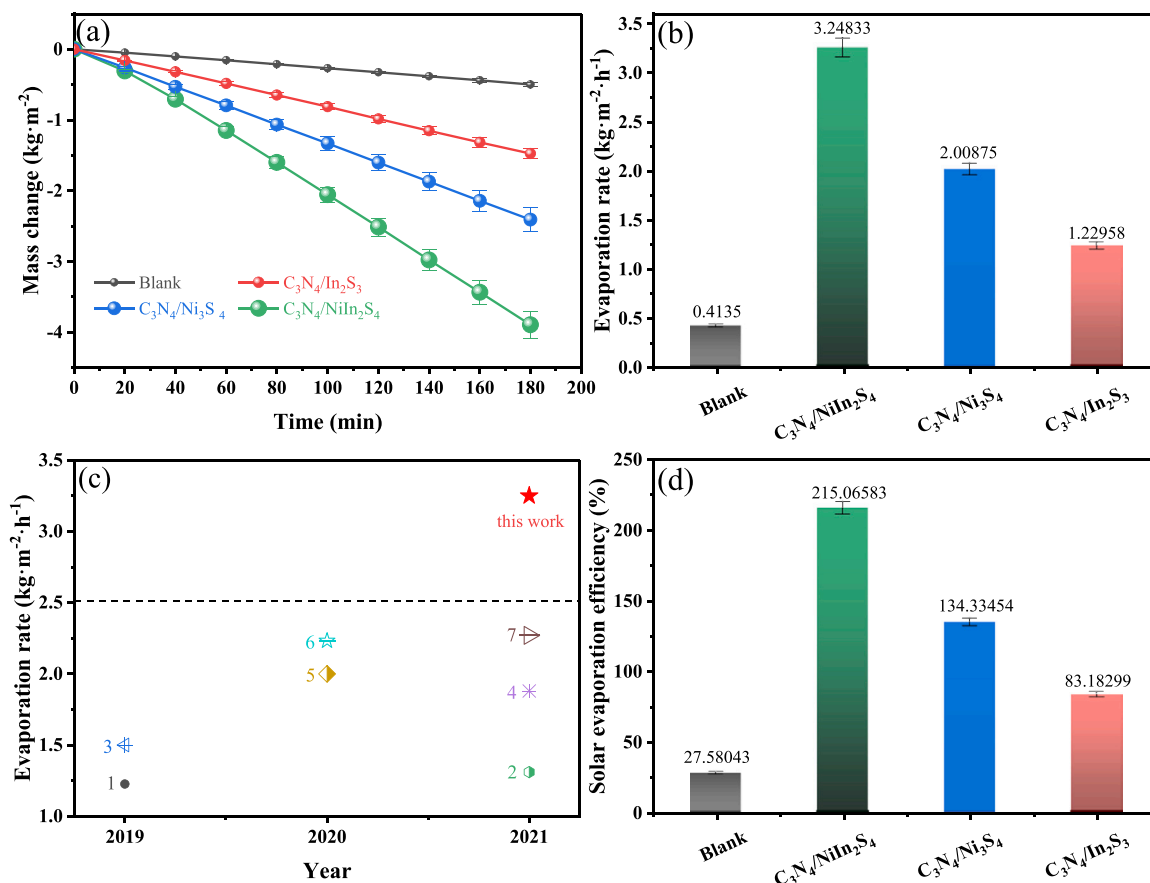
Fig. 4. Mass change curves of evaporated water for samples prepared at one sun intensity (a); The rate of evaporation of water from the prepared samples at one sun intensity (b); Comparison graph of evaporation rate of powder sample solar water (1 [35], 2 [36], 3 [37], 4 [38], 5 [39], 6 [40], 7 [41]) (c) and the solar water evaporation efficiency of the prepared samples (d).

conduction band participates in the oxygen reduction reaction. There are two types of ORRs possible in this process, one is the two-electron reduction of O_2 in one step to produce H_2O_2 (Eq. 5), and the other is the single-electron reduction of O_2 in two steps to produce H_2O_2 (Eq. 6 & Eq. 7). Fig. 5c shows the EIS Nyquist plots of the samples, where the $C_3N_4/NiIn_2S_4$ has the smallest arc radius. This indicates that $C_3N_4/NiIn_2S_4$ has a low electrical resistance, suggesting that this composite has the highest capacity for photoinduced charge carrier separation, correlated with increased photocatalytic activity accordingly. To investigate the carrier transfer and separation processes in the photocatalysts, a photoelectrochemical analysis was also performed. As seen from Fig. 5d, compared with other samples, $C_3N_4/NiIn_2S_4$ showed a strong photocurrent response, indicating that an effective photoinduced charge transfer occurred between $NiIn_2S_4$ and C_3N_4 (Fig. 5d). To verify the cycling stability of $C_3N_4/NiIn_2S_4$ in the experiment, six cycles of H_2O_2 generation experiments were performed under the same conditions. As shown in Fig. S7, it is clear that the performance of photocatalytic H_2O_2 production on $C_3N_4/NiIn_2S_4$ is quite stable, implying that the structural stability of $C_3N_4/NiIn_2S_4$ complex in water is good.

Due to the addition of $NiIn_2S_4$, the band gap of $C_3N_4/NiIn_2S_4$ composite is reduced, which greatly enhances its light absorption range and absorption intensity, thus enabling efficient absorption of sunlight and photothermal conversion. The transition metal Ni exists in the $C_3N_4/NiIn_2S_4$ composite in the form of variable valence oxidation state, which facilitates the transport of photogenerated carriers. Moreover, the composite of C_3N_4 and $NiIn_2S_4$ forms a heterogeneous structure, which greatly enhances the photogenerated carrier generation efficiency. In addition, the porous structure of $C_3N_4/NiIn_2S_4$ composite can provide more catalytic active sites, which is favorable for the photocatalytic

generation of H_2O_2.

4. Conclusions

In this work, $C_3N_4/NiIn_2S_4$ composites were obtained by the solvothermal method. The diffraction peaks, composition, morphology, and chemical states of the composites were characterized by X-ray diffraction, X-ray photoelectron spectroscopy and scanning electron microscopy. The experimental results show that the prepared $C_3N_4/NiIn_2S_4$ nanomaterials cannot only absorb sunlight well, convert it into thermal energy, increase the material interface temperature and promote water evaporation, but also achieve a water evaporation rate of $3.25~kg \cdot m^{-2} \cdot h^{-1}$ under the irradiation of one sunlight intensity. And it also has the ability of photocatalytic output of H_2O_2, which can produce $1080~\mu mol^{-1} \cdot L^{-1}$ of H_2O_2 in one hour under the irradiation of visible light. We believe that this multi-functional catalyst material will provide a simple and sustainable development strategy for the cleanup of water resources and the production of new resources.

Author contributions

All authors contributed to the writing of this manuscript and agreed on the final version of the manuscript.

CRediT authorship contribution statement

Anhu Wang: Conceptualization, Methodology, Investigation, Writing – original draft. **Huagen Liang**: Conceptualization, Validation, Resources, Writing – review & editing. **Fu Chen**: Methodology, Writing
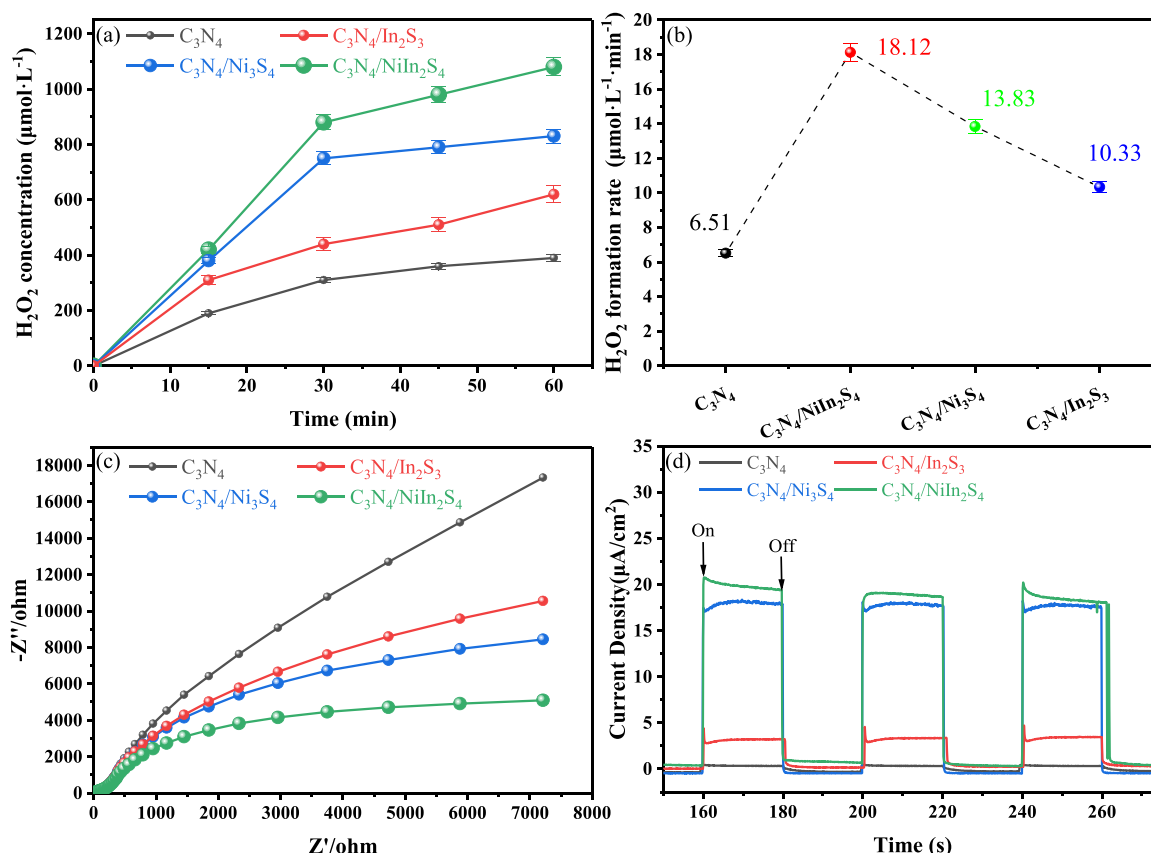
Fig. 5. The photocatalytic production of H_2O_2 from the prepared samples under the irradiation of one solar light intensity (a); The rate of H_2O_2 production from the prepared samples (b); EIS spectra (c), and transient photocurrent spectra (d) of the prepared samples.

Declaration of Competing Interest

The authors declare that they have no known competing financial interests or personal relationships that could have appeared to influence the work reported in this paper.

Appendix A. Supporting information

Supplementary data associated with this article can be found in the online version at doi:10.1016/j.apcatb.2022.121336.

References

[1] R. Fuoco, S. Giannarelli, Integrity of aquatic ecosystems: an overview of a message from the South Pole on the level of persistent organic pollutants (POPs), Microchem. J. 148 (2019) 230–239.

[2] F. Zhao, Y.H. Guo, X.Y. Zhou, W. Shi, G.H. Yu, Materials for solar-powered water evaporation, Nat. Rev. Mater. 5 (2020) 388–401.

[3] P. Tao, G. Ni, C.Y. Song, W. Shang, J.B. Wu, J. Zhu, G. Chen, T. Deng, Solar-driven interfacial evaporation, Nat. Energy 3 (2018) 1031–1041.

[4] L.L. Zhu, M.M. Gao, C.K.N. Peh, G.W. Ho, Recent progress in solar-driven interfacial water evaporation: advanced designs and applications, Nano Energy 57 (2019) 507–518.

[5] X.Q. Li, J.L. Li, J.Y. Lu, N. Xu, C.L. Chen, X.Z. Min, B. Zhu, H.X. Li, L. Zhou, S. N. Zhu, T.J. Zhang, J. Zhu, Enhancement of interfacial solar vapor generation by environmental energy, Joule 2 (2018) 1331–1338.

[6] X.M. Ma, S. He, B. Qiu, F. Luo, L.H. Guo, Z.Y. Lin, Noble metal nanoparticle-based multicolor immunoassays: an approach toward visual quantification of the analytes with the naked eye, ACS Sens. 4 (2019) 782–791.

[7] L.N. Ding, Y. Chang, P.F. Yang, W.H. Gao, M.M. Sun, Y.M. Bie, L. Yang, X.M. Ma, Y. M. Guo, Facile synthesis of biocompatible L-cysteine-modified MoS2 nanospheres with high photothermal conversion efficiency for photothermal therapy of tumor, Mater. Sci. Eng. C. -Mater. Biol. Appl. 117 (2020), 111371.

[8] X.Y. Liu, X.Y. Li, Y. Shan, Y.X. Yin, C.R. Liu, Z. Lin, S.S. Kumar, CuS nanoparticles anchored to g-C3N4 nanosheets for photothermal ablation of bacteria, RSC Adv. 10 (2020) 12183–12191.

[9] J. Farkasovska, V. Bugarova, J. Godocikova, V. Majtan, J. Majtan, The role of hydrogen peroxide in the antibacterial activity of different floral honeys, Eur. Food Res. Technol. 245 (2019) 2739–2744.

[10] X.J. Guo, Y.A. Xu, K.B. Wang, F. Zha, X.H. Tang, H.F. Tian, Synthesis of magnetic CuFe2O4 self-assembled hollow nanospheres and its application for degrading methylene blue, Res. Chem. Intermed. 46 (2020) 853–869.

[11] H. Ye, S. Lu, Effect of hydrogen peroxide on the structure and photocatalytic activity of titania, Res. Chem. Intermed. 41 (2015) 139–149.

[12] J.M. Campos-Martin, G. Blanco-Brieva, J.L.G. Fierro, Hydrogen peroxide synthesis: an outlook beyond the anthraquinone process, Angew. Chem. Int. Ed. 45 (2006) 6962–6984.

[13] H.X. Zhang, S.C. Yang, Y.L. Wang, J.C. Xi, J.C. Huang, J.F. Li, P. Chen, R. Jia, Electrocatalyst derived from fungal hyphae and its excellent activity for electrochemical production of hydrogen peroxide, Electro Acta 308 (2019) 74–82.

[14] M.M. Momeni, M. Akbarnia, Photoelectrochemical, photocatalytic and electrochemical hydrogen peroxide production using Fe/S-codoped TiO2 nanotubes as new visible-light-absorbing photocatalysts, Appl. Phys. A-Mater. Sci. Process. 127 (2021) 449.

[15] Y. Guo, Y.J. Jin, H.M. Wu, D.X. Li, X.F. Fan, L.D. Zhou, X.F. Zhang, Direct synthesis of propylene oxide using hydrogen peroxide in a membrane reactor, Chem. Pap. 71 (2017) 49–57.

[16] S. Fukuzumi, Y.M. Lee, W. Nam, Solar-driven production of hydrogen peroxide from water and dioxygen, Chem. -A Eur. J. 24 (2018) 5016–5031.

[17] M.H. Sun, X.G. Wang, Z.Q. Chen, M. Murugananthan, Y. Chen, Y.R. Zhang, Stabilized oxygen vacancies over heterojunction for highly efficient and exceptionally durable VOCs photocatalytic degradation, Appl. Catal. B: Environ. 273 (2020), 119061.

[18] M. Sun, X. Wang, Y. Li, H. Pan, M. Murugananthan, Y. Han, J. Wu, M. Zhang, Y. Zhang, Z. Kang, Bifunctional Pd-O$_x$ center at the liquid-solid-gas triphase interface for H$_2$O$_2$ photosynthesis, ACS Catal. 12 (2022) 2138–2149.

[19] H.Y. Shi, Y. Li, X.F. Wang, H.G. Yu, J.G. Yu, Selective modification of ultra-thin g-C$_3$N$_4$ nanosheets on the (110) facet of Au/BiVO$_4$ for boosting photocatalytic H$_2$O$_2$ production, Appl. Catal. B: Environ. 297 (2021), 120414.

[20] H. Pan, M. Sun, X. Wang, M. Zhang, M. Murugananthan, Y. Zhang, A novel electric-assisted photocatalytic technique using self-doped TiO$_2$ nanotube films, Appl. Catal. B: Environ. 307 (2022), 121174.

[21] H.L. Hou, X.K. Zeng, X.W. Zhang, Production of hydrogen peroxide by photocatalytic processes, Angew. Chem. Int. Ed. 59 (2020) 17356–17376.

[22] Q.M. Gan, Y.Y. Xiao, C.X. Li, H. Peng, T.Q. Zhang, M.M. Ye, g-C$_3$N$_4$/MoS$_2$ based floating solar still for clean water production by thermal/light activation of persulfate, Chemosphere 280 (2021), 130618.

[23] Y. Peng, L. Zhou, L. Wang, J. Lei, Y. Liu, S. Daniele, J. Zhang, Preparation of NiCoP-decorated g-C$_3$N$_4$ as an efficient photocatalyst for H$_2$O$_2$ production, Res. Chem. Intermed. 45 (2019) 5907–5917.

[24] B. Liu, C. Bie, Y. Zhang, L. Wang, Y. Li, J. Yu, Hierarchically porous ZnO/g-C$_3$N$_4$ S-scheme heterojunction photocatalyst for efficient H$_2$O$_2$ production, Langmuir 37 (2021) 14114–14124.

[25] Y.Z. Wu, J. Ward-Bond, D.L. Li, S.H. Zhang, J.F. Shi, Z.Y. Jiang, g-C$_3$N$_4$@α-Fe$_2$O$_3$/C photocatalysts: synergistically intensified charge generation and charge transfer for NADH regeneration, ACS Catal. 8 (2018) 5664–5674.

[26] L.J. Wu, J.W. Lang, P. Zhang, X. Zhang, R.S. Guo, X.B. Yan, Mesoporous Ni-doped MnCo$_2$O$_4$ hollow nanotubes as an anode material for sodium ion batteries with ultralong life and pseudocapacitive mechanism, J. Mater. Chem. A 4 (2016) 18392–18400.

[27] G.T. Fu, J. Wang, Y.F. Chen, Y. Liu, Y.W. Tang, J.B. Goodenough, J.M. Lee, Exploring indium-based ternary thiospinel as conceivable high-potential air-cathode for rechargeable Zn-Air batteries, Adv. Energy Mater. 8 (2018), 1802263.

[28] G.T. Fu, Y. Wang, Y.W. Tang, K. Zhou, J.B. Goodenough, J.M. Lee, Superior oxygen electrocatalysis on nickel indium thiospinels for rechargeable zn-air batteries, ACS Mater. Lett. 1 (2019) 123–131.

[29] S. Dou, L. Tao, J. Huo, S.Y. Wang, L.M. Dai, Etched and doped Co$_9$S$_8$/graphene hybrid for oxygen electrocatalysis, Energy Environ. Sci. 9 (2016) 1320–1326.

[30] Y. Cui, C.W. Zhou, X.Z. Li, Y. Gao, J. Zhang, High performance electrocatalysis for hydrogen evolution reaction using nickel-doped CoS$_2$ nanostructures: experimental and DFT insights, Electro Acta 228 (2017) 428–435.

[31] S.C. Huang, Y.Y. Meng, S.M. He, A. Goswami, Q.L. Wu, J.H. Li, S.F. Tong, T. Asefa, M.M. Wu, N-, O-, and S-tridoped carbon-encapsulated Co$_9$S$_8$ nanomaterials: efficient bifunctional electrocatalysts for overall water splitting, Adv. Funct. Mater. 27 (2017), 1606585.

[32] T.Y. Ma, Y.H. Tang, S. Dai, S.Z. Qiao, Proton-functionalized two-dimensional graphitic carbon nitride nanosheet: an excellent metal-/label-free biosensing platform, Small 10 (2014) 2382–2389.

[33] M.Z. Li, G.H. Wu, Z.H. Liu, X.Y. Xi, Y. Xia, J. Ning, D. Yang, A.G. Dong, Uniformly coating ZnAl layered double oxide nanosheets with ultra-thin carbon by ligand and phase transformation for enhanced adsorption of anionic pollutants, J. Hazard. Mater. 397 (2020), 122766.

[34] J. Feng, T.T. Chen, S.N. Liu, Q.H. Zhou, Y.M. Ren, Y.Z. Lv, Z.J. Fan, Improvement of g-C$_3$N$_4$ photocatalytic properties using the Hummers method, J. Colloid Interface Sci. 479 (2016) 1–6.

[35] P.F. Wang, Y.F. Gu, L. Miao, J.H. Zhou, H. Su, A.Y. Wei, X.J. Mu, Y.Z. Tian, J. Q. Shi, H.F. Cai, Co$_3$O$_4$ nanoforest/Ni foam as the interface heating sheet for the efficient solar-driven water evaporation under one sun, Sustain. Mater. Technol. 20 (2019), e00106..

[36] J.L. Wang, W.K. Wang, X.Y. Mu, Z.T. Li, C.B. Wang, Hexagonal cluster Mn-MOF nanoflowers with super-hydrophilic properties for efficient and continuous solar-driven clean water production, Sustain. Energy Fuels 5 (2021) 1905–2002.

[37] X.C. Zhang, X.N. Wang, W.D. Wu, X.D. Chen, Z.X. Wu, Self-floating monodisperse microparticles with a nano-engineered surface composition and structure for highly efficient solar-driven water evaporation, J. Mater. Chem. A 7 (2019) 6963–6971.

[38] Z. Qin, H. Sun, Y.N. Tang, S.Y. Yin, L.X. Yang, M.W. Xu, Z.N. Liu, Bioinspired hydrophilic-hydrophobic janus composites for highly efficient solar steam generation, ACS Appl. Mater. Interfaces 13 (2021) 19467–19475.

[39] H.F. Yang, G.C. Yang, Z.Q. Qiao, H.B. Bao, S.T. Zhang, X.M. Li, Y.S. Liu, Facile deflagration synthesis of hollow carbon nanospheres with efficient performance for solar water evaporation, ACS Appl. Mater. Interfaces 12 (2020) 35193–35200.

[40] Q. Zhang, L.P. Ren, X.F. Xiao, Y.L. Chen, L.J. Xia, G.M. Zhao, H.J. Yang, X.B. Wang, W.L. Xu, Vertically aligned Juncus effusus fibril composites for omnidirectional solar evaporation, Carbon 156 (2020) 225–233.

[41] D. Li, S.S. Chen, R.R. Huang, C.R. Xue, P.F. Li, Y.S. Li, Q. Chang, H.Q. Wang, N. Li, S.P. Jia, S.L. Hu, J.L. Yang, Photothermal, photocatalytic, and anti-bacterial Ti-Ag-O nanoporous powders for interfacial solar driven water evaporation, Ceram. Int. 47 (2021) 19800–19808.

[42] Z.Y. Xu, L.N. Zhang, L. Zhao, B.J. Li, B. Bhatia, C.X. Wang, K.L. Wilke, Y. Song, O. Labban, J.H. Lienhard, R.Z. Wang, E.N. Wang, Ultrahigh-efficiency desalination via a thermally-localized multistage solar still, Energy Environ. Sci. 13 (2020) 830–839.

[43] Y. Zhang, Y. Xia, L.X. Wang, B. Cheng, J.G. Yu, Influence of calcination temperature on photocatalytic H$_2$O$_2$ productivity of hierarchical porous ZnO microspheres, Nanotechnology 32 (2021), 415402.